Supplement of Geosci. Model Dev., 17, 7767–7793, 2024
https://doi.org/10.5194/gmd-17-7767-2024-supplement
© Author(s) 2024. CC BY 4.0 License.

Geoscientific Model Development
Open Access
EGU

Supplement of

A fully coupled solid-particle microphysics scheme for stratospheric aerosol injections within the aerosol–chemistry–climate model SOCOL-AERv2

Sandro Vattioni et al.

Correspondence to: Sandro Vattioni (sandro.vattioni@env.ethz.ch)

The copyright of individual parts of the supplement might differ from the article licence.

S1 Discrete Element Model Simulations

We have performed DEM simulations to quantify the resulting mobility radius of the agglomerates represented in the solid particle microphysics scheme. The model (Kelesidis and Kholghy, 2021) was run under a initial concentrations spanning 5 to 6 orders of magnitude with primary particle radius of 5 nm, 80 nm and 215 nm for alumina particles and 5 nm, 80 nm and 275 nm for calcite particles (see Figure S1). We assumed that a global injection rate of 5 Mt/yr could be achieved with 200 airplane flights per day, each with a flight distance of 1000 km in the stratosphere and by assuming each airplane injecting a total of 69 t of particles from two injectors of which both have a square area of 1 m^2. This would result in an initial concentration of about 2×10^{13} particles per cm^3 when injecting 5 nm particles, 4×10^{12} particles per cm^3 when injecting particles at a primary radius of 80 nm and about about 1×10^{8} particles per cm^3 when injecting particles at a radius of 240 nm. Figure S1 shows the resulting number concentration as a function of time, while the DEM did not account for dilution of the air parcel with time, which would additionally reduce the resulting number density with time significantly. Since the simulations run for a fixed amount of computational time, the simulations with lower initial concentrations and larger primary radius and thus less coagulation resulted in simulation of a longer time period. The resulting size distribution at the end of each simulation is shown in Figure S2. Most initial concentrations for alumina particles of radius 215 nm and calcite particles of radius 275 nm result in size distributions peaking at agglomerates of 10^{1} to 10^{3} monomers per agglomerate, which would result in significantly decreased back scatter efficiencies and increased sedimentation rates for injection of alumina particles with radius of 215 nm and calcite particles with radius of 275 nm particles. At this injection radii, only the lowest initial concentration of 10^5 particles per cm^3 would result in 20% of the alumina particles and about 50% of the calcite particles remaining as monomers. This initial concentration is 3 orders of magnitudes less than the initial assumption derived from injection of 200 airplane flights per day stated above. It is still an open question whether taking into account dilution of air would reduce the formation of larger agglomerates for 80 nm particle injection and 215 nm or 275 nm particle injection to a level, which does not result in agglomerates with significantly reduced back scatter efficiency or significantly increased sedimentation speeds.

Figure S3 shows the mobility radius of the agglomerates resulting from the DEM simulations. The resulting radii are slightly larger compared to the coated alumina particles assuming a fractal dimension of 2.6 in Weisenstein et al. (2015, see their equation 1) and significantly smaller compared to their pure alumina radii with fractal dimension of 1.6.

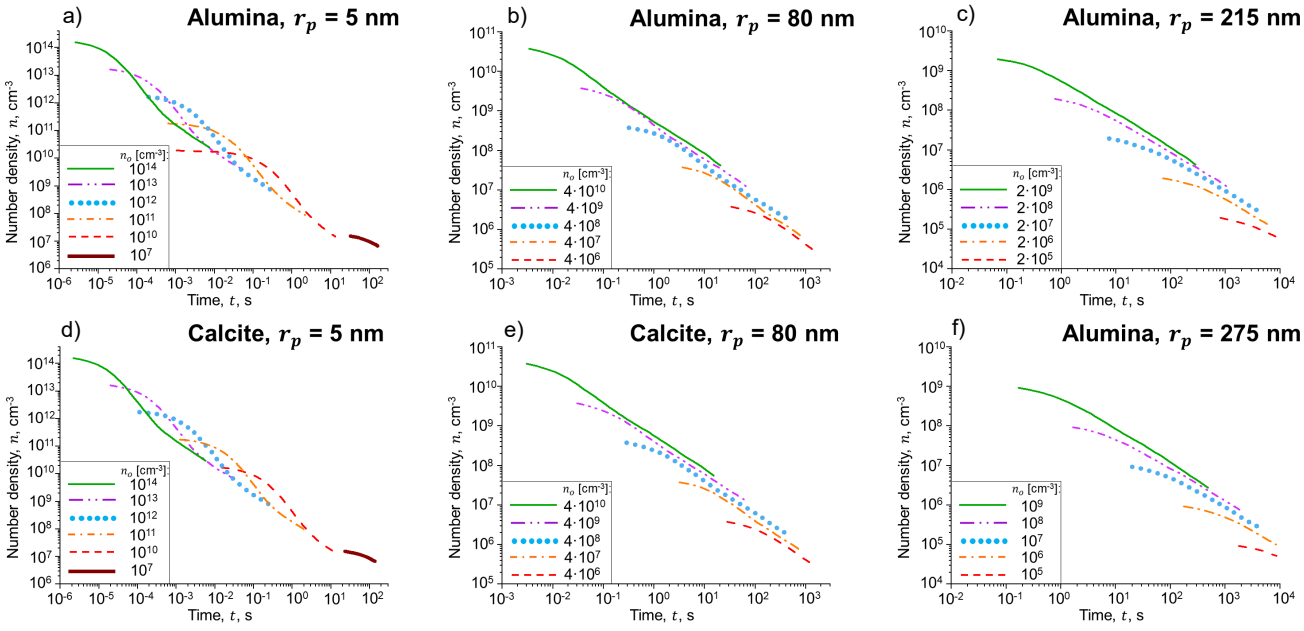

Figure S1. The evolution of the total particle number density as a function of time assuming different initial number concentrations of particles with radii of 5 nm (a and d), 80 nm (b and e) as well as 215 nm (for alumina, c) and 275 nm (for calcite, f) simulated with a DEM (Kelesidis et al., 2021).

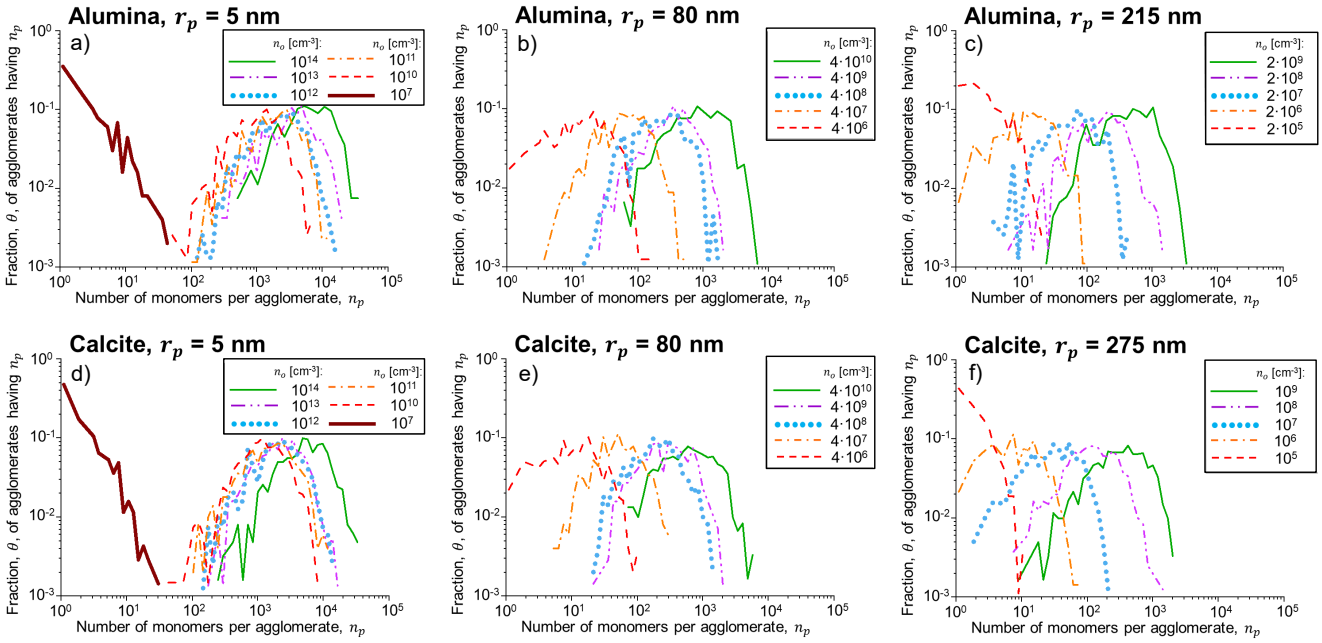

Figure S2. The resulting size distribution at the end of the simulations resulting from coagulation with different initial concentrations of particles with radii of 5 nm (a and d), 80 nm (b and e) as well as 215 nm (for alumina, c) and 275 nm (for calcite, f) simulated with a DEM (Kelesidis et al., 2021). Depicted size distribution are the one resulting at the end of the simulations shown in Figure S1. The model does not account for dilution, which would reduce the number densities with time.

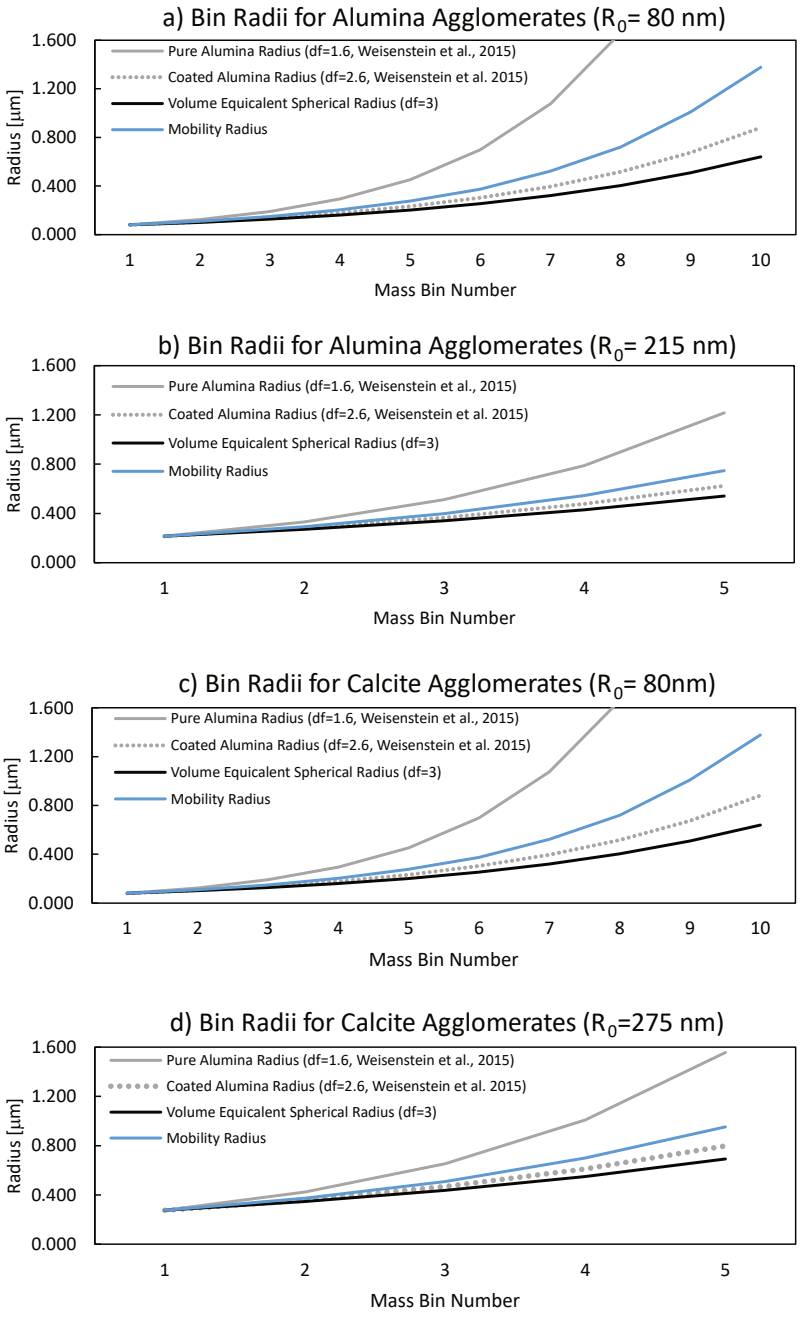

Figure S3. Different radii for the agglomerates of primary particle radius of 80 nm (a) and 215 nm (b) for alumina particles as well as of 80 nm (c) and 275 nm (d) for calcite particles. Shown are calculated agglomerate radii applied in Weisenstein et al. (2015, see their equation 1) with fractal dimensions of 1.6 for their bare alumina particles (gray solid line) and 2.6 for their coated alumina particles (grey stippled line), the resulting mobility radii from the DEM simulations (blue), which are used in this study, as well as the volume equivalent radii (black) for reference.

S2 Sedimentation velocities in SOCOL-AERv2

The resulting calculated aerosol sedimentation velocities in SOCOL-AERv2 are slightly smaller than in Weisenstein et al. (2015), but compare generally well within the stratosphere (see Figure S4), while some deviations occur in the troposphere which might be due the three dimensional resolution of the dynamics in SOCOL-AERv2 compared to 2D-AER.

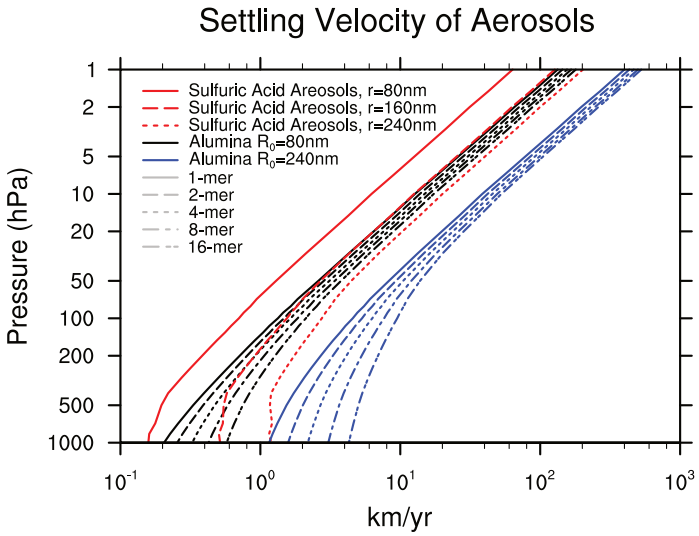

Figure S4. The sedimentation velocities calculated by SOCOL-AERv2 with equation 4 in the main text zonally averaged between 15°N and 15°S over 15 years.

S3 Optical Properties used in SOCOL-AERv2

Figure S5 shows the absorption cross sections (σ_{abs}) for all spectral bands as well as the scattering cross section (σ_{sca}) and the asymmetry factors (g_{asy}) for the shortwave (SW) bands of SOCOL-AERv2 for alumina and calcite particles as well as for 70 wt% H_2SO_4 aerosols of monomer radii of 80 nm, 160 nm, 240 nm and 320 nm. To get the absorption and scattering cross sections, the scattering and absorption efficiencies (Q_{abs} and Q_{sca}), which were derived from Mie theorie (Mätzler, 2002; Rannou et al., 1999), were multiplied with $r^2_{\text{ve},i}$ (see Section "Radiation" in the main text). Calcite particles show a relatively large absorption in the visible and UV wavelengths, whereas sulfuric acid and alumina particles only absorb little SW radiation (Figure S5a). In the longwave (LW) bands, sulfuric acid is showing the largest absorption except for the bands 700-800 cm^{-1} and 1390-1480 cm^{-1} where alumina and calcite particles absorb more LW radiation, respectively compared to sulfuric acid aerosols. While the absorption peak for alumina is at the edge of the CO_2 absorption band ($\sim$7 μm) close to the atmospheric window of outgoing LW radiation, the peak for the calcite particles is in the tail of the outgoing LW radiation spectra within the water absorption band where outgoing LW radiation is absorbed anyway ($\sim$13.3 μm). Therefore, SAI of alumina particles is likely resulting in more stratospheric warming compared to calcite particles. Figure S6 shows the optical properties derived with the semi-empirical code from Rannou et al. (1999) fed into SOCOL-AERv2 for agglomerates. The absorption cross sections in Figure S5 and S6 are largest for 80 nm particles and monomers, respectively. However, this is only valid on a per particle basis. Normalized per mass the particles would all show similar absorption coefficients since absorption is proportional to mass (see Figure S5 c). The scattering cross section (Figure S5d) is largest for 320 nm particles and lowest for 80 nm particles. However, 320 nm particles also result in smallest stratospheric aerosol burden since they sediment faster. The asymmetry factor (Figure S5b) is also generally largest for 320 nm particles and sulfuric acid aerosols in the visible band between 440 nm and 690 nm and lowest for alumina particles. A large asymmetry factor stands for a large forward scattering fraction. The larger the agglomerate the larger the scattering cross section and the larger the asymmetry factor, which results in more forward scattering.

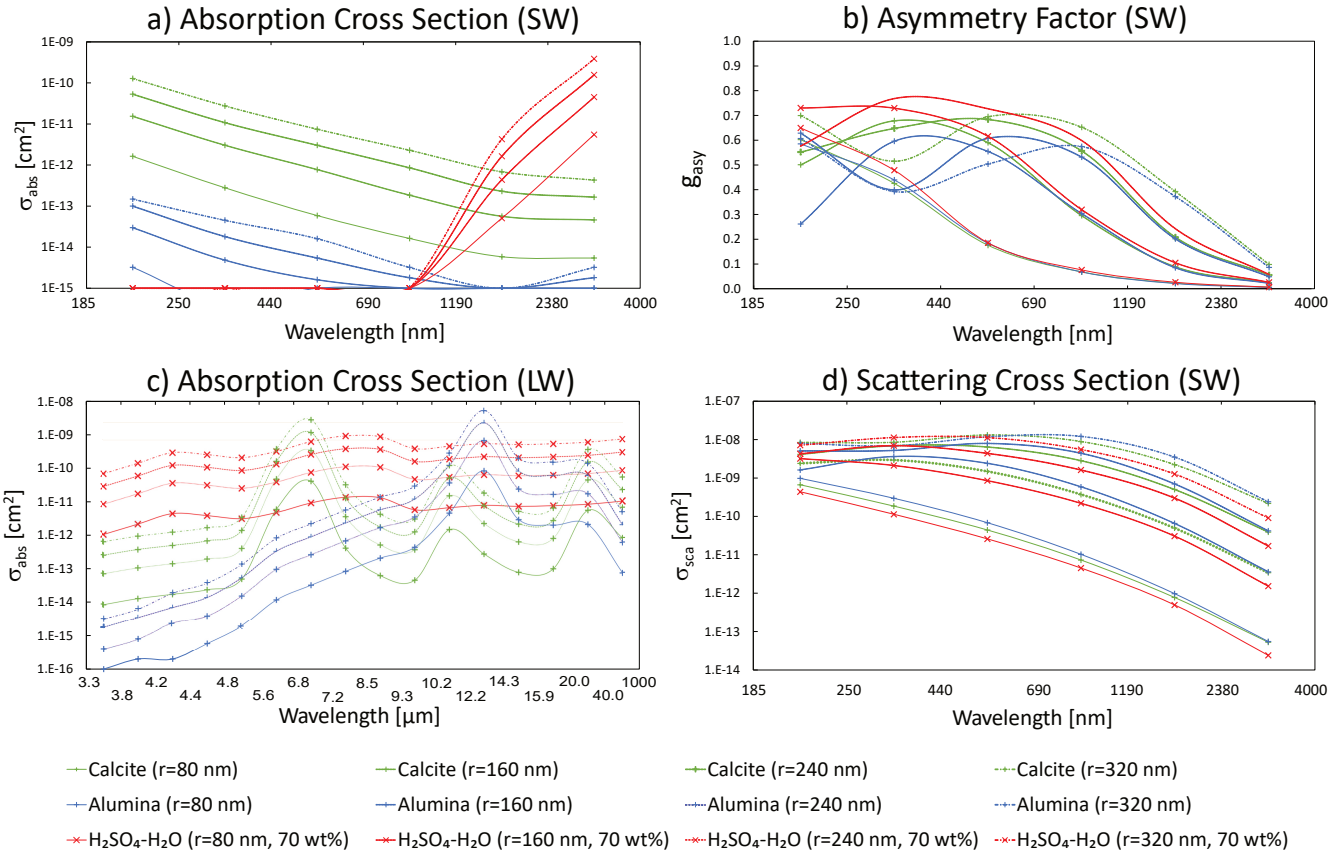

Figure S5. Shown are the absorption cross section for the SW bands (a), the asymmetry factor for the SW bands (b), the absorption cross section of the LW bands (c) as well as the scattering cross section for the SW bands (d) for alumina and calcite monomers with primary radius of 80 nm, 160 nm, 240 nm and 320 nm. The optical properties were derived with the code of Mätzler (2002). As a reference, the optical properties for sulfuric acid aerosols used in SOCOL-AERv2, which are based on Yue et al. (1994) and Biermann et al. (1996) are also shown for aerosols with 70 wt% sulfuric acid.

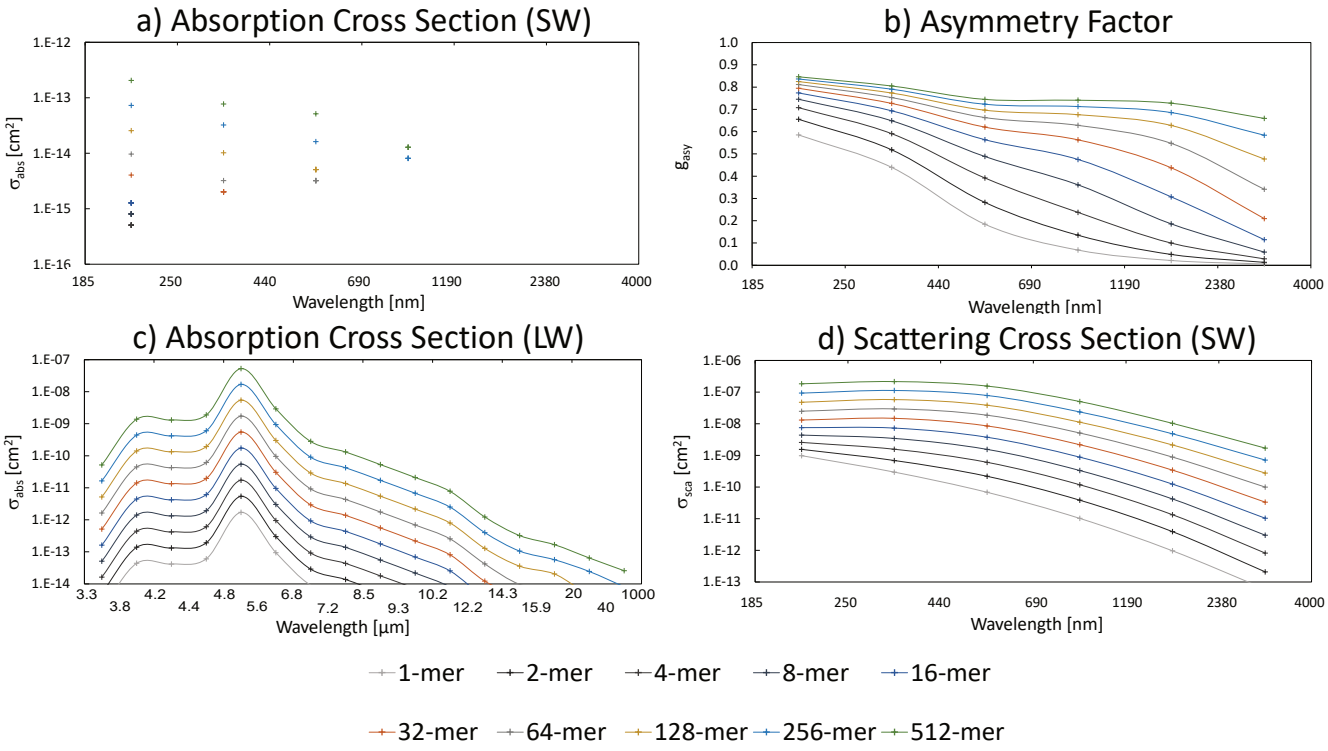

Figure S6. Shown are the optical properties of alumina particles with 80 nm parimary radius as well as of the corresponding agglomerates up to 512-mers implemented in SOCOL-AERv2. Optical properties for agglomerates were derived using the semi-empirical code of Rannou et al. (1999). Shown are the absorption cross section for the SW bands (a), the asymmetry factor for the SW bands (b), the absorption cross section of the LW bands (c) as well as the scattering cross section for the SW bands (d).

S4 Stratospheric aerosol size distributions

The stratospheric aerosol size distribution for the injection scenarios of 5 Mt/yr calcite particles (r=240 nm), alumina particles (r=240 nm), SO_2, and AM$-H_2SO_4$ (r=0.95 µm and σ=1.5). The size distributions clearly indicate a decrease in sulfuric acid particle concentrations in the solid particle injection scenarios. The calcite particles result in slightly larger agglomeration due to larger stratospheric aerosol burden and a smaller density which makes coagulation more efficient compared to alumina particle emission. It can also be seen that the sulfuric acid aerosol size distributions resulting from AM$-H_2SO_4$ result in larger number concentrations between 0.1 µm and 0.2 µm radius, which explains the larger net TOA radiative forcing despite the slightly lower stratospheric aerosol burden (see Figure 4 in the main text).

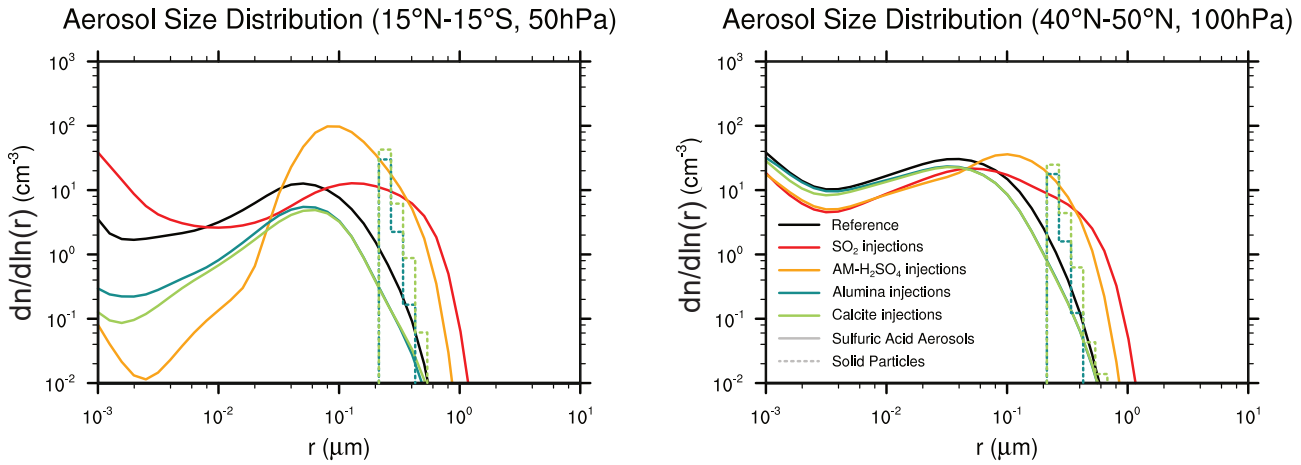

Figure S7. The resulting aerosol size distribution averaged between 15°N and 15°S at 50 hPa altitude (a) and between 40°N and 50°N at 100 hPa altitude (b). Solid lines show the sulfuric acid aerosol size distribution and dashed lines the solid particle size distributions for the 5 Mt/yr injection scenarios as well as the reference simulation (black).

S5 The stratospheric sulphur cycle under different alumina injection rates

Figure S8 shows the stratospheric sulfur cycle response to injection of alumina particles with radii of 240 nm at different injection rates. The response of the stratospheric sulfur cycle is proportional to the available solid particle surface area density (SAD), which increases for larger injection rates. Therefore the response of the stratospheric sulfur cycle when increasing the injection rate while keeping the alumina particle radius constant is the same as when decreasing the particle radius at constant injection rate (see Figure 6 in the main text). Figure S9 shows the corresponding sulfuric acid coating thickness if the sulfuric acid was distributed equally on the alumina particles. If the aerosol burden is very small (i.e., 1 Mt/yr in Figure S9a) the coating thickness could be up to 44 nm in the lower stratosphere, whereas the thickness would only be 2-4 nm for injection of 25 Mt/yr of alumina particles with radii of 240 nm.

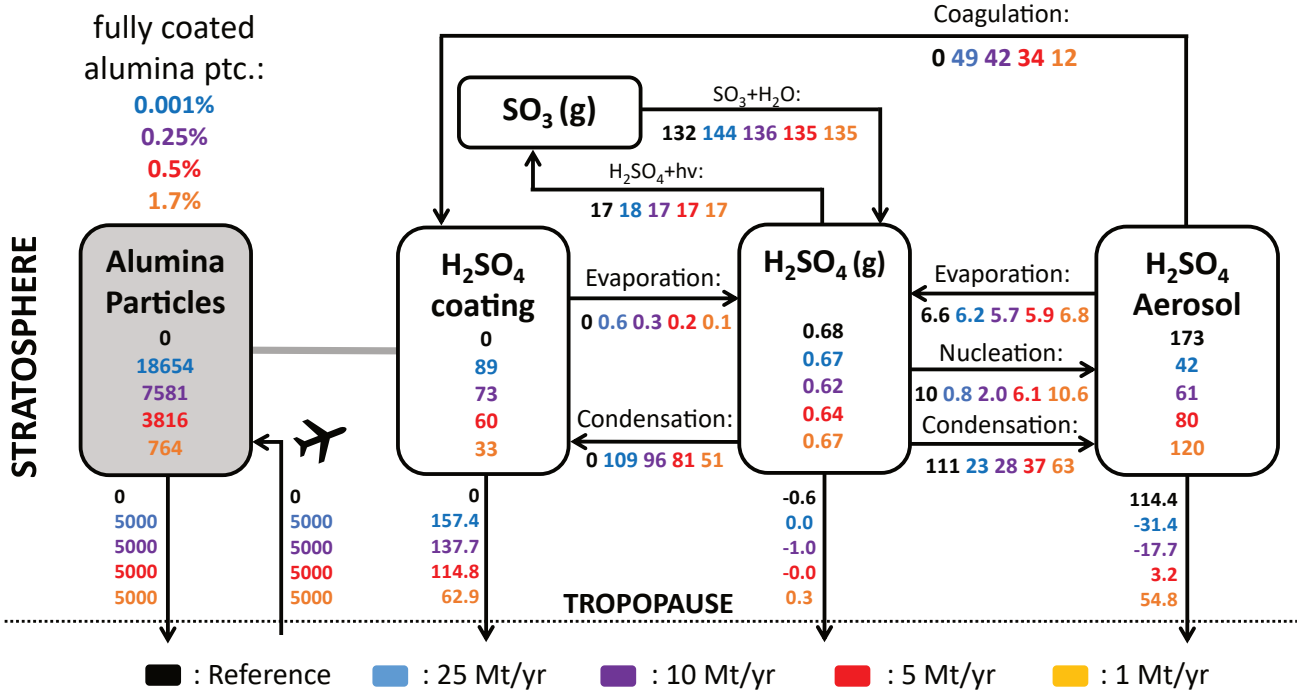

Figure S8. The stratospheric sulfur cycle under conditions of SAI with particles at radii of 240 nm and injection rates of 25 Mt/yr (blue), 10 Mt/yr (violet), 5 Mt/yr (red) and 1 Mt/yr (orange). All sulfur species are shown in Gg Sulrur for burden (boxes) and Gg Sulfur per year for net fluxes (arrows). The alumina burden (gray box) is given as Gg Al_2O_3 and Gg Al_2O_3 per year. Net cross tropopause fluxes are calculated by balancing the stratospheric mass fluxes of the individual species.

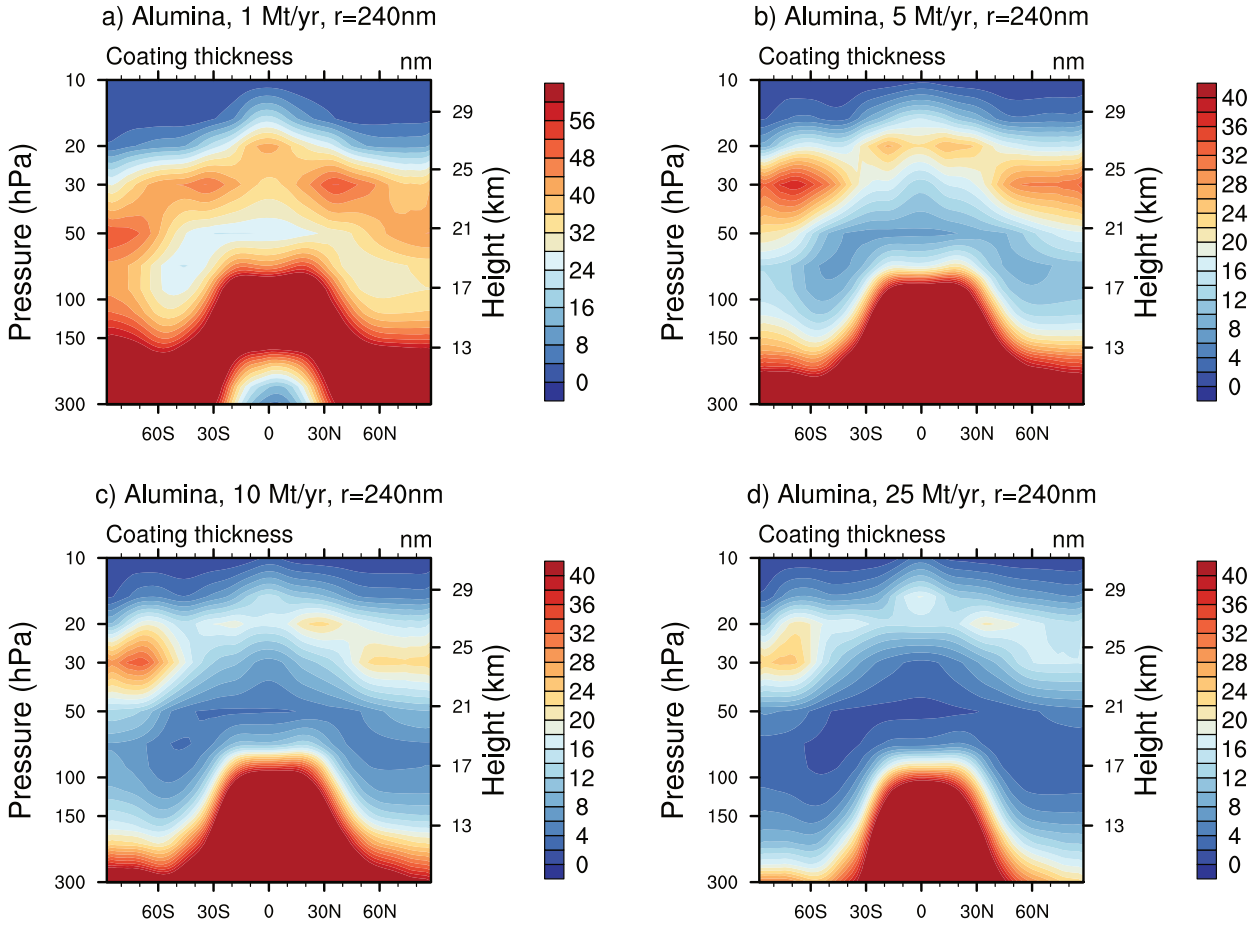

Figure S9. The resulting coating thickness when injecting alumina particles with radii of 240 nm at 1 Mt/yr (a), 5 Mt/yr (b), 10 Mt/yr (c) and 25 Mt/yr (d). The values listed above correspond to the average coating sickness of the mass bin with the largest coating thickness, which is at the same time also the mass bin with the largest share of alumina burden (bin 1 for all scenarios). Other mass bin have smaller coating thicknesses.

S6 The stratospheric sulphur cycle under different calcite injection rates

Figure S10 shows the response of the stratospheric sulfur cycle to different injection rates of calcite particles. The response of the stratospheric sulfur cycle is proportional to the available solid particle SAD, which increases for larger injection rates. Therefore the response of the stratospheric sulfur cycle when increasing the calcite particle injection rate while keeping the radius constant is the same as for decreasing the particle radius at constant injection rate (see Figure 9 in the main text). The larger the available solid particle SAD the larger the uptake of H_2SO_4, HCl and HNO_3.

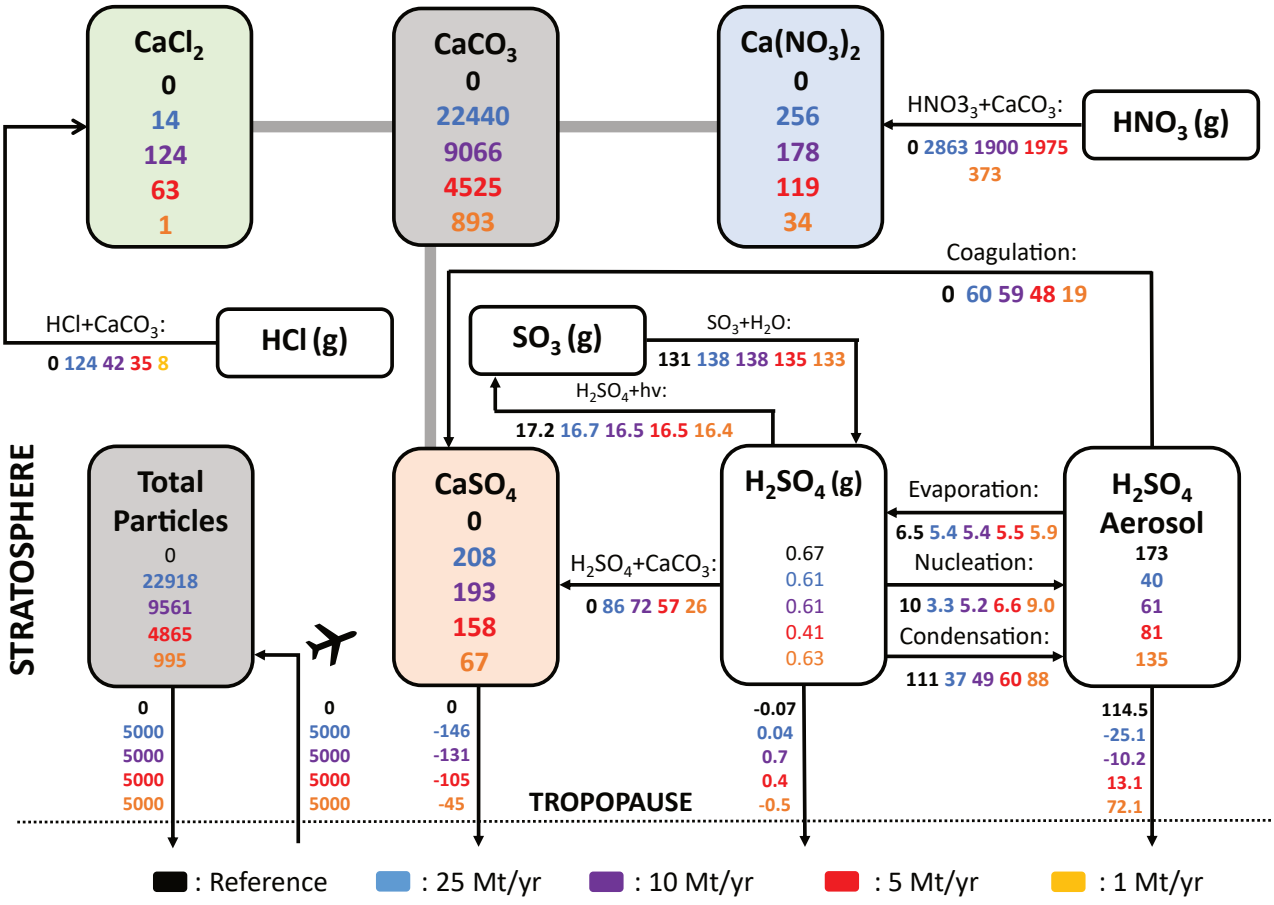

Figure S10. The stratospheric sulfur cycle under conditions of SAI of calcite particles with radii of 240nm and injection rates of 25 Mt/yr (blue), 10 Mt/yr (violet), 5 Mt/yr (red) and 1 Mt/yr (orange). All sulfur species (except $CaSO_4$) are shown in Gg Sulrur for burden (boxes) and Gg Sulfur per year for net fluxes (arrows). The solid species (colored boxes) are given in Gg of the corresponding material. The HNO_3 and HCl flux to $Ca(NO_3)_2$ and $CaCl_2$ are given in Gg HNO_3 per year and Gg HCl per year. Cross tropopause fluxes are calculated by balancing the mass balance of the individual species.

S7 Number concentrations and surface area densities for calcite particles

Figure S11 shows the resulting number concentrations and the resulting calcite SAD for various calcite injection scenarios. As resulting stratospheric aerosol burden for calcite particle injections are about 25% larger for compared to alumina particle injection, also the resulting number concentrations and solid particle SAD are larger. Figure 10 in the main text shows the corresponding figure for alumina particles.

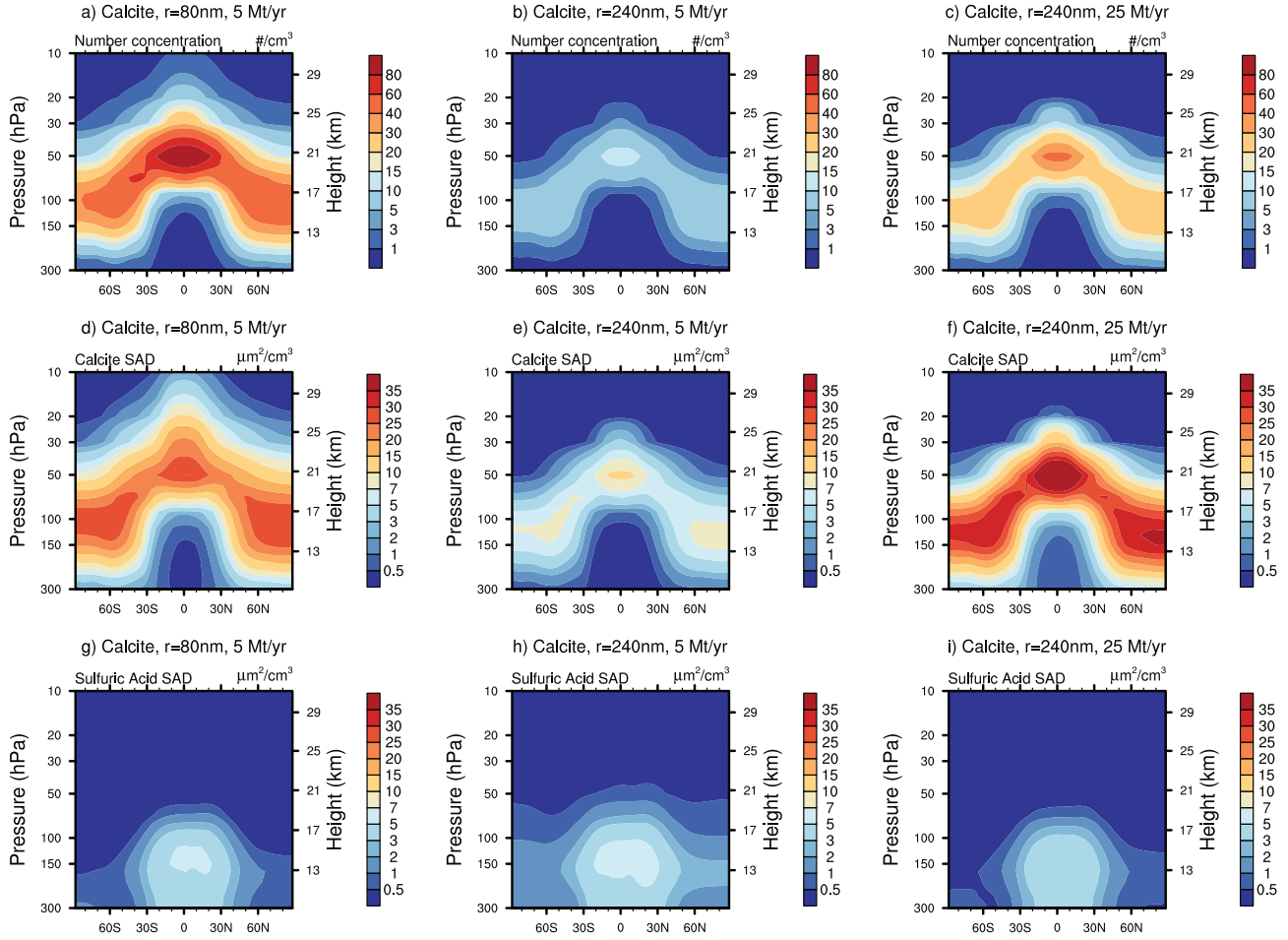

Figure S11. The resulting zonal mean number densities (a-c), calcite SAD (d-f) and sulfuric acid SAD (g-i) from injection of 5 Mt/yr of particles with 80 nm (a,d,f), 5 Mt/yr of particles with 240 nm particles (b,e,h) and 25 Mt/yr of particles with 240 nm radius (c,f,i).

References

Biermann, U. M., Presper, T., Koop, T., Mößinger, J., Crutzen, P. J., and Peter, T.: The unysuitability of meteoritic and other nuclei for polar stratospheric cloud freezing, Geophysical Research Letters, 23, 1693–1696, https://doi.org/10.1029/96GL01577, 1996.

Kelesidis, G. A. and Kholghy, M. R.: A Monodisperse Population Balance Model for Nanoparticle Agglomeration in the Transition Regime, Materials, 14, https://doi.org/10.3390/ma14143882, 2021.

Mätzler, C.: MATLAB functions for Mie scattering and absorption, version 2, https://boris.unibe.ch/146550/1/199.pdf, 2002.

Rannou, P., McKay, C., Botet, R., and Cabane, M.: Semi-empirical model of absorption and scattering by isotropic fractal aggregates of spheres, Planetary and Space Science, 47, 385–396, https://doi.org/10.1016/S0032-0633(99)00007-0, 1999.

Weisenstein, D. K., Keith, D. W., and Dykema, J. A.: Solar geoengineering using solid aerosol in the stratosphere, Atmos. Chem. Phys., 15, 11 835–11 859, https://doi.org/10.5194/acp-15-11835-2015, 2015.

Yue, G., Poole, L., Wang, P.-H., and Chiou, E.: Stratospheric aerosol acidity, density, and refractive index deduced from SAGE II and NMC temperature data, Journal of Geophysical Research: Atmospheres, 99, 3727–3738, https://doi.org/10.1029/93JD02989, 1994.